Unified Load-Independent ZPA Analysis and Design in CC and CV Modes of Higher Order Resonant Circuits for WPT Systems

Jianghua Lu, *Student Member, IEEE*, Guorong Zhu, *Senior Member, IEEE*, Deyan Lin, *Member, IEEE*, Yiming Zhang, *Member, IEEE*, Jin Jiang, *Fellow, IEEE*, and Chunting Chris Mi, *Fellow, IEEE*

***Abstract*— This article proposes a general unified methodology for arbitrary higher order resonant circuits. With the proposed methodology, the equivalent circuits and the general resonant methods of the higher order resonant circuit are presented to realize the load-independent constant current (CC) and constant voltage (CV) outputs at two different load-independent zero phase angle (ZPA) frequencies. In addition, the corresponding regularized mathematical models of the constant output current and voltage and the purely resistive input impedances in CC and CV output modes are derived. All compensation topologies in both inductive and capacitive power transfer (CPT) systems have the essence of higher order resonant circuits. It means that the proposed methodology can be applied to investigate the load-independent output and input characteristics of any inductive power transfer (IPT) and CPT topologies. A 3.3-kW LCC-series-compensated IPT system for electric vehicles (EVs) was designed and manufactured to verify the theoretical analysis. The system operating frequencies in both the CC output with ZPA and the CV output with ZPA are in compliance with the SAE J2954 standard.**

***Index Terms*— Capacitive power transfer (CPT), constant current/constant voltage (CC/CV) charging, electric vehicle (EV), higher order resonant circuit, inductive power transfer (IPT), L-section matching network, unity power factor.**

I. Introduction

THE wireless power transfer (WPT) technology [1], [2] is becoming widely used in cardiac pacemakers, mobile phones, drones, lighting, and electric vehicles (EVs) [3]–[5]. In a wireless EV charging system, to ensure the safety, durability, and performance of the battery, a constant current/constant voltage (CC/CV) charging profile, regardless of the variation of the battery state of charge (SOC), is one of the most essential characteristics [6]–[8]. Besides, to enhance the power transfer capability, diminish the volt–ampere (VA) rating, and ensure soft-switching operating condition of the primary inverter, the zero phase angle (ZPA), namely unit power factor, between the primary inverter output current and voltage is necessary [8]–[10].

Usually, a downstream dc–dc converter or a variable frequency control [11] is adopted to regulate the battery load-independent CC or CV output characteristic. However, the additional converter inevitably increases the component counts and associated power losses and costs. For the variable frequency control, the ZPA condition or slightly inductive input impedance is difficult to be achieved over the full range of the charging mode. To achieve load-independent CC output with ZPA or load-independent CV output with ZPA, an inductive power transfer (IPT) topology with a ZPA frequency-tracking control and a back-end converter is proposed [10]. As mentioned previously, however, the additional converter will make the power receiver system bulky and inefficient. Additionally, instability issues due to the frequency bifurcation phenomenon may be inevitable for the ZPA frequency-tracking control [12].

However, the method of designing specified resonant conditions for the compensation topologies in IPT and capacitive power transfer (CPT) systems is an alternative solution. In the IPT systems, the CC output mode at a ZPA frequency can be obtained for the series–series (S-S) [13]–[15], S-CLC [16], double-sided LCL [17], [18], or double-sided LCC [15], [19]–[21]. Moreover, the series–parallel (S-P) [14], double-sided LCC [20], [21], and S-SP [22], [23] compensation topologies can realize load-independent CV outputs with ZPA. For these various compensation topologies, however, the analysis and design of the resonant methods are different and irregular. So, a general and simplified method that can systematically analyze the CC and/or CV outputs with ZPA is necessary to be compatible with all kinds of compensation topologies in wireless EV charging applications. In [24] and [25], methods using the basic LC network, T-network, and π-network are proposed to investigate the load-independent CC and CV output characteristics of arbitrary topologies. However, the ZPA condition in CC or CV mode needs further comprehensive analysis. In order to analyze the CC output with ZPA operation or the CV output with

Manuscript received February 10, 2019; revised June 7, 2019; accepted August 29, 2019. Date of publication September 11, 2019; date of current version January 7, 2020. This work was supported in part by the Scholarship from the China Scholarship Council and in part by the National Natural Science Foundation of China under Grant 51777146 and Grant 51977163. *(Corresponding author: Chunting Chris Mi.)*

J. Lu, G. Zhu, and D. Lin are with the School of Automation, Wuhan University of Technology, Wuhan 430070, China (e-mail: tri_ljh@whut.edu.cn; zhgr_55@whut.edu.cn; deyanlin@whut.edu.cn).

Y. Zhang and C. C. Mi are with the Department of Electrical and Computer Engineering, San Diego State University, San Diego, CA 92182 USA (e-mail: zhangym07@gmail.com; cmi@sdsu.edu).

J. Jiang is with the Department of Electrical and Computer Engineering, The University of Western Ontario, London, ON N6A 3K7, Canada (e-mail: jjiang@eng.uwo.ca).

Digital Object Identifier 10.1109/TTE.2019.2940337

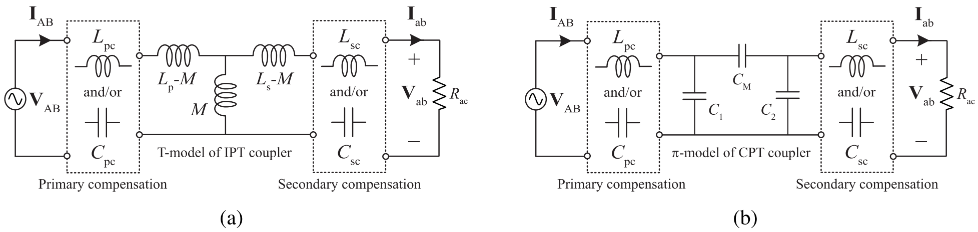

Fig. 1. General configurations of (a) IPT systems and (b) CPT systems.

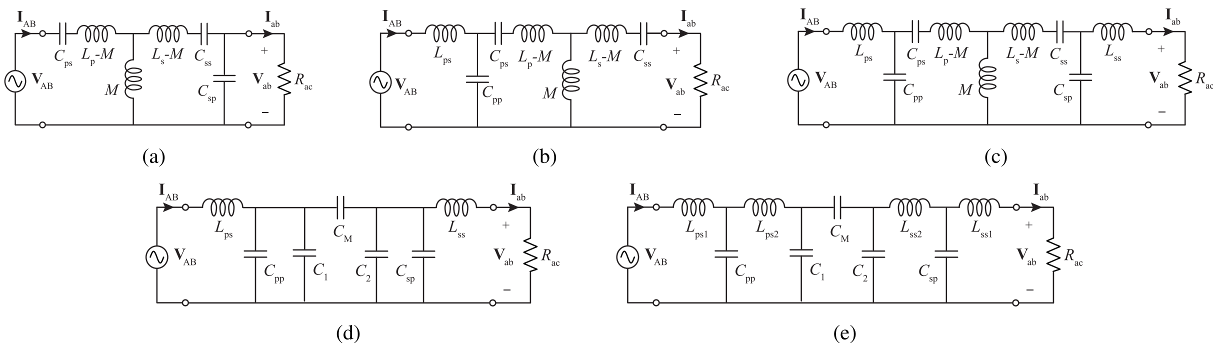

Fig. 2. Some widely used compensation topologies in IPT and CPT systems. (a) S-SP-compensated IPT topology [22], [23]. (b) LCC-series-compensated IPT topology [31], [32]. (c) Double-sided LCC-compensated IPT topology [15], [19]–[21]. (d) Double-sided LC-compensated CPT topology [27]. (e) Double-sided $LCLC$-compensated CPT topology [33], [34].

ZPA operation of any compensation topologies, a graphical approach method [26] and a family of higher order resonant circuits [16] are proposed. But it is difficult to simultaneously analyze the load-independent CC and CV output modes both with ZPA of arbitrary compensation circuits.

In the CPT systems, there is a paucity of literature on the load-independent output current and voltage and the input ZPA characteristics. The load-independent CC and CV output modes are analyzed and designed for the double-sided LC compensation [27]. In [28], primary π-CLC and secondary T-CLC compensation topologies are proposed to achieve the load-independent CC output mode at a ZPA frequency, while the CV output is realized at a non-ZPA frequency. To promote the application of CPT systems in EVs, more research about the general method analyzing the load-independent CC and CV output modes both with ZPA is also necessary.

To address the aforementioned issues, what we desire, in this article, to accomplish for the dozen compensation topologies in wireless EV charging applications are as follows:

1) a general and simplified method that analyze the load-independent CC and CV outputs with ZPA conditions of arbitrary higher order resonant circuits including some widely used compensation topologies in both IPT and CPT systems;
2) the regularized mathematical models that express the load-independent output current and voltage and the purely resistive input impedances in CC and CV charging modes.

Specifically, Section II describes the detailed equivalent circuits for an arbitrary higher order resonant circuit and derives the mathematical models. The application of the proposed method in the IPT system is given in Section III. In Section IV, the analytical results are experimentally evaluated. The conclusions are summarized in Section V.

II. Load-Independent CC and CV Output Modes With ZPA Conditions of Higher Order Resonant Circuits

A. Fundamental of Wireless Power Transfer System

The general configurations of the IPT system [16], [29] and CPT system [30] are shown in Fig. 1(a) and (b), respectively. In the IPT system, the loosely coupled transformer with the primary and secondary coils is modeled as its T-model. L_{p} and L_{s} represent the primary and secondary self-inductances, and M is the mutual inductance. R_{ac} is an ac load. The capacitive coupler in the CPT system is equivalent to its π-model [30]. In IPT and CPT systems, L_{pc} and/or C_{pc} represent the primary compensation components and L_{sc} and/or C_{sc} are the secondary compensation components. Fig. 2 shows some widely used compensation topologies in IPT and CPT systems, for example, an LCC-series-compensated IPT topology [31], [32] shown in Fig. 2(b). From Figs. 1 and 2, it can be seen that all IPT and CPT systems have the essence of higher order resonant circuits.

Fig. 3 shows a general higher order resonant circuit, where X_{S1}, X_{S2}, …, $X_{\mathrm{S(m-1)}}$, and X_{Sm} represent the series reactances and X_{P1}, X_{P2}, …, and $X_{\mathrm{P(m-1)}}$ represent the parallel reactances. "j" is the unit imaginary number.

B. Basic L-Section Matching Networks

As shown in Fig. 4(a) and (b), respectively, the reversed and normal L-section matching networks [35] are the two types of the most basic resonant circuit. X_{1R} and X_{2R} are the two reactances of the reversed L-section network, and X_{1N} and X_{2N} are the reactances of the normal L-section network.

The output current of the reversed L-section network ($\mathbf{I}_{\mathrm{abR}}$) and the output voltage of the normal L-section network ($\mathbf{V}_{\mathrm{abN}}$)

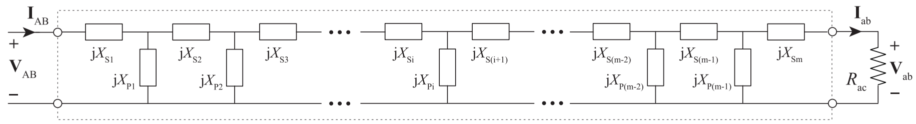

Fig. 3. Arbitrary higher order resonant circuit.

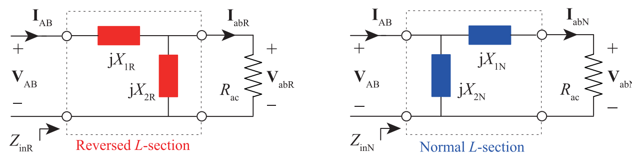

(a) (b)

Fig. 4. (a) Reversed L-section matching network. (b) Normal L-section matching network.

are derived as

$$\mathbf{I}_{\mathrm{abR}} = \frac{\mathrm{j}X_{2\mathrm{R}}}{R_{\mathrm{ac}}\cdot(\mathrm{j}X_{1\mathrm{R}}+\mathrm{j}X_{2\mathrm{R}})+\mathrm{j}X_{1\mathrm{R}}\cdot\mathrm{j}X_{2\mathrm{R}}}\mathbf{V}_{\mathrm{AB}} \quad (1)$$

$$\mathbf{V}_{\mathrm{abN}} = \frac{R_{\mathrm{ac}}\cdot\mathrm{j}X_{2\mathrm{N}}}{R_{\mathrm{ac}}+\mathrm{j}X_{1\mathrm{N}}+\mathrm{j}X_{2\mathrm{N}}}\mathbf{I}_{\mathrm{AB}} \quad (2)$$

where $\mathbf{V}_{\mathrm{AB}}$ and $\mathbf{I}_{\mathrm{AB}}$ are the phasors of the input-port voltage and current.

In addition, the input impedances of the reversed and normal L-section matching networks are expressed as

$$Z_{\mathrm{inR}} = \frac{R_{\mathrm{ac}}\cdot\mathrm{j}X_{2\mathrm{R}}}{R_{\mathrm{ac}}+\mathrm{j}X_{2\mathrm{R}}}+\mathrm{j}X_{1\mathrm{R}} = \frac{R_{\mathrm{ac}}(\mathrm{j}X_{1\mathrm{R}}+\mathrm{j}X_{2\mathrm{R}})-X_{1\mathrm{R}}X_{2\mathrm{R}}}{R_{\mathrm{ac}}+\mathrm{j}X_{2\mathrm{R}}} \quad (3)$$

$$Z_{\mathrm{inN}} = \frac{(R_{\mathrm{ac}}+\mathrm{j}X_{1\mathrm{N}})\mathrm{j}X_{2\mathrm{N}}}{(R_{\mathrm{ac}}+\mathrm{j}X_{1\mathrm{N}})+\mathrm{j}X_{2\mathrm{N}}} = \frac{(R_{\mathrm{ac}}+\mathrm{j}X_{1\mathrm{N}})\mathrm{j}X_{2\mathrm{N}}}{R_{\mathrm{ac}}+(\mathrm{j}X_{1\mathrm{N}}+\mathrm{j}X_{2\mathrm{N}})}. \quad (4)$$

In (1) and (2), when

$$X_{1\mathrm{R}}+X_{2\mathrm{R}} = 0 \quad (5)$$

$$X_{1\mathrm{N}}+X_{2\mathrm{N}} = 0. \quad (6)$$

$\mathbf{I}_{\mathrm{abR}}$ and $\mathbf{V}_{\mathrm{abN}}$ are independent of the load R_{ac} and can be simplified as

$$\mathbf{I}_{\mathrm{abR}} = \frac{1}{\mathrm{j}X_{1\mathrm{R}}}\mathbf{V}_{\mathrm{AB}} = \frac{1}{-\mathrm{j}X_{2\mathrm{R}}}\mathbf{V}_{\mathrm{AB}} \quad (7)$$

$$\mathbf{V}_{\mathrm{abN}} = \mathrm{j}X_{2\mathrm{N}}\mathbf{I}_{\mathrm{AB}} = -\mathrm{j}X_{1\mathrm{N}}\mathbf{I}_{\mathrm{AB}}. \quad (8)$$

Moreover, under the conditions of (5) and (6), Z_{inR} and Z_{inN} are, respectively, given by

$$Z_{\mathrm{inR}} = \frac{-X_{1\mathrm{R}}X_{2\mathrm{R}}}{R_{\mathrm{ac}}+\mathrm{j}X_{2\mathrm{R}}} \quad (9)$$

$$Z_{\mathrm{inN}} = \frac{(R_{\mathrm{ac}}+\mathrm{j}X_{1\mathrm{N}})\mathrm{j}X_{2\mathrm{N}}}{R_{\mathrm{ac}}}. \quad (10)$$

For the higher order resonant circuit shown in Fig. 3, the following criteria hold.

1) The parallel reactances X_{P1} to $X_{\mathrm{P(m\text{-}2)}}$ in Fig. 3 are modeled as the parallel connection of two reactances, i.e., X_{Pi} is expressed by using X_{PiC1} and X_{PiC2} in parallel. The corresponding equivalent variables are expressed by (11).

2) The series reactances X_{S2} to $X_{\mathrm{S(m\text{-}1)}}$ are equivalent to the series connection of two reactances, i.e., X_{Si} is expressed by X_{SiC1} and X_{SiC2} in series, which is derived in (12)

$$\mathrm{j}X_{\mathrm{Pi}} = \frac{\mathrm{j}X_{\mathrm{PiC1}}\mathrm{j}X_{\mathrm{PiC2}}}{\mathrm{j}X_{\mathrm{PiC1}}+\mathrm{j}X_{\mathrm{PiC2}}}, \quad \mathrm{i}\in\{1,2,\ldots,(\mathrm{m}-2)\} \quad (11)$$

$$\mathrm{j}X_{\mathrm{Si}} = \mathrm{j}X_{\mathrm{SiC1}}+\mathrm{j}X_{\mathrm{SiC2}}, \quad \mathrm{i}\in\{1,2,\ldots,(\mathrm{m}-1)\}. \quad (12)$$

Fig. 3 is modeled as cascaded connection of (m-1)-stage reversed L-section networks (marked with the red components) and (m-2)-stage normal L-section networks (marked with the blue components), which is shown in Fig. 5(a).

Similarly, the higher order resonant circuit shown in Fig. 3 can also be modeled as shown in Fig. 5(b), and the corresponding variables are expressed as

$$\mathrm{j}X_{\mathrm{Pi}} = \frac{\mathrm{j}X_{\mathrm{PiV1}}\mathrm{j}X_{\mathrm{PiV2}}}{\mathrm{j}X_{\mathrm{PiV1}}+\mathrm{j}X_{\mathrm{PiV2}}} \text{ and}$$

$$\mathrm{j}X_{\mathrm{Si}} = \mathrm{j}X_{\mathrm{SiV1}}+\mathrm{j}X_{\mathrm{SiV2}}, \quad \mathrm{i}\in\{1,2,\ldots,(\mathrm{m}-1)\}. \quad (13)$$

It can be seen that the equivalent circuit shown in Fig. 5(b) consists of (m-1)-stage reversed L-section and (m-1)-stage normal L-section in series.

From Fig. 5(a) and (b), an arbitrary higher order resonant circuit can be modeled as cascaded connection of one or more stages of reversed L-section matching networks and one or more stages of normal L-section matching networks. It means that the two basic types of L-section matching networks can be applied to simplify the analysis and design of the output and input characteristics of any higher order resonant circuits.

C. General Load-Independent CC Output Mode With Load-Independent ZPA

According to the analysis of the reversed and normal L-section matching networks, when the sums of the two reactances of all L-section networks in Fig. 5(a) are designed to be equal to zero, namely,

$$\begin{aligned} & X_{\mathrm{S1}}+X_{\mathrm{P1C1}} \\ & = X_{\mathrm{P1C2}}+X_{\mathrm{S2C1}} = X_{\mathrm{S2C2}}+X_{\mathrm{P2C1}} = \cdots \\ & = X_{\mathrm{SiC2}}+X_{\mathrm{PiC1}} = X_{\mathrm{PiC2}}+X_{\mathrm{S(i+1)C1}} = \cdots \\ & = X_{\mathrm{P(m-2)C2}}+X_{\mathrm{S(m-1)C1}} = X_{\mathrm{S(m-1)C2}}+X_{\mathrm{P(m-1)}} \\ & = 0 \end{aligned} \quad (14)$$

and the transconductance $\mathbf{G}_{\mathrm{CC}}$ of Fig. 5(a) can be expressed as

$$\begin{aligned} \mathbf{G}_{\mathrm{CC}} &= \frac{\mathbf{I}_{\mathrm{ab\_CC}}}{\mathbf{V}_{\mathrm{AB}}} \\ &= \frac{\mathrm{j}X_{\mathrm{P1C2}}}{\mathrm{j}X_{\mathrm{S1}}}\frac{\mathrm{j}X_{\mathrm{P2C2}}}{\mathrm{j}X_{\mathrm{S2C2}}}\cdots\frac{\mathrm{j}X_{\mathrm{PiC2}}}{\mathrm{j}X_{\mathrm{SiC2}}} \\ &\quad \cdots\frac{\mathrm{j}X_{\mathrm{P(m-2)C2}}}{\mathrm{j}X_{\mathrm{S(m-2)C2}}}\frac{1}{\mathrm{j}X_{\mathrm{S(m-1)C2}}} \end{aligned} \quad (15)$$

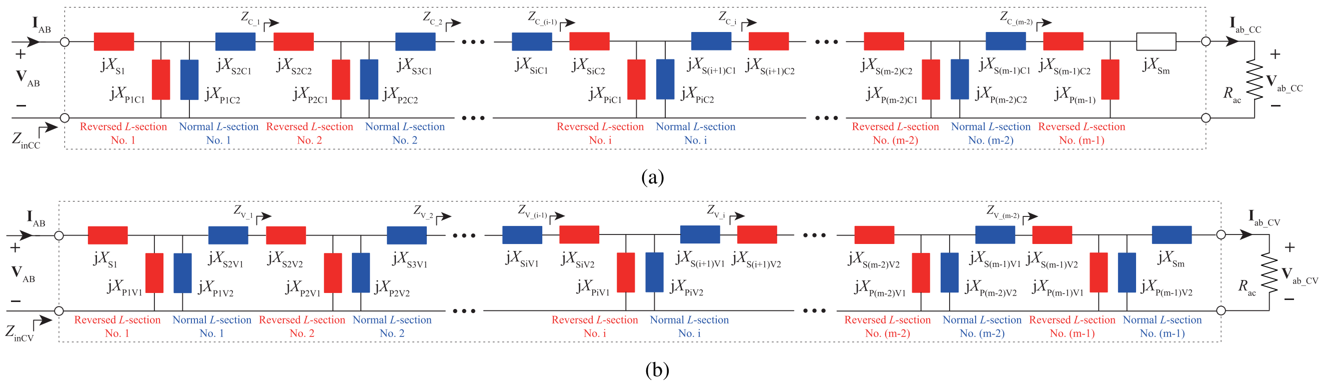

Fig. 5. Two different equivalent circuits of an arbitrary higher order resonant circuit. (a) Equivalent circuit for achieving the CC output with ZPA. (b) Equivalent circuit for achieving the CV output with ZPA.

$$\begin{aligned}
X_{\rm S1} &= -X_{\rm P1C1} = X_{\rm R_C_1} (\text{for reversed } L\text{-section No. 1})\\
X_{\rm P1C2} &= -X_{\rm S2C1} = X_{\rm N_C_1} (\text{for normal } L\text{-section No. 1})\\
X_{\rm S2C2} &= -X_{\rm P2C1} = X_{\rm R_C_2}\\
X_{\rm P2C2} &= -X_{\rm S3C1} = X_{\rm N_C_2}\\
&\vdots\\
X_{\rm SiC2} &= -X_{\rm PiC1} = X_{\rm R_C_i} (\text{for reversed } L\text{-section No. i})\\
X_{\rm PiC2} &= -X_{\rm S(i+1)C1} = X_{\rm N_C_i} (\text{for normal } L\text{-section No. i})\\
&\vdots\\
X_{\rm S(m-1)C2} &= -X_{\rm P(m-1)} = X_{\rm R_C_(m-1)}. \qquad (16)
\end{aligned}$$

From (15), $\mathbf{G}_{\rm CC}$ is independent of the load. It means that the load-independent CC output is obtained when the higher order resonant circuit is fed by a CV supply and resonates at the conditions of (14).

In order to simplify and express the regularity of the load-independent CC output characteristic, we define the unified nomenclature of all the variables in Fig. 5(a) as (16) according to (14). In (16), $X_{\rm R\_C\_i}$ and $X_{\rm N\_C\_i}$ represent the unified reactances of the i reversed and normal L-section networks, respectively.

Then, the load-independent $\mathbf{G}_{\rm CC}$ can be simplified to

$$\begin{aligned}
\mathbf{G}_{\rm CC} &= \frac{\mathbf{I}_{\rm ab_CC}}{\mathbf{V}_{\rm AB}}\\
&= \frac{X_{\rm N_C_1}}{X_{\rm R_C_1}} \cdots \frac{X_{\rm N_C_i}}{X_{\rm R_C_i}} \cdots \frac{X_{\rm N_C_(m-2)}}{X_{\rm R_C_(m-2)}} \frac{1}{{\rm j}X_{\rm R_C_(m-1)}}\\
&= \frac{\prod\limits_{\rm i=1}^{\rm (m-2)} X_{\rm N_C_i}}{{\rm j}\prod\limits_{\rm i=1}^{\rm (m-1)} X_{\rm R_C_i}}. \qquad (17)
\end{aligned}$$

Furthermore, according to (9), (10), and (16), the input impedance of Fig. 5(a) ($Z_{\rm inCC}$) is expressed as

$$\begin{aligned}
Z_{\rm inCC} &= {\rm Re}(Z_{\rm inCC}) + {\rm j}\cdot{\rm Im}(Z_{\rm inCC}) = R_{\rm inCC} + {\rm j}\cdot X_{\rm inCC}\\
&= \frac{-X^2_{\rm R_C_1}}{\dfrac{(Z_{\rm C_1} - {\rm j}X_{\rm N_C_1})\cdot {\rm j}X_{\rm N_C_1}}{Z_{\rm C_1}} - {\rm j}X_{\rm R_C_1}} \qquad (18)
\end{aligned}$$

where

$$\begin{aligned}
Z_{\rm C_1} &= \frac{-X^2_{\rm R_C_2}}{\dfrac{(Z_{\rm C_2} - {\rm j}X_{\rm N_C_2})\cdot {\rm j}X_{\rm N_C_2}}{Z_{\rm C_2}} - {\rm j}X_{\rm R_C_2}}\\
&\vdots\\
Z_{\rm C_i} &= \frac{-X^2_{\rm R_C_(i+1)}}{\dfrac{(Z_{\rm C_(i+1)} - {\rm j}X_{\rm N_C_(i+1)})\cdot {\rm j}X_{\rm N_C_(i+1)}}{Z_{\rm C_(i+1)}} - {\rm j}X_{\rm R_C_(i+1)}}\\
&\vdots\\
Z_{\rm C_(m-3)} &= \frac{-X^2_{\rm R_C_(m-2)}}{\dfrac{(Z_{\rm C_(m-2)} - {\rm j}X_{\rm N_C_(m-2)})\cdot {\rm j}X_{\rm N_C_(m-2)}}{Z_{\rm C_(m-2)}} - {\rm j}X_{\rm R_C_(m-2)}}\\
Z_{\rm C_(m-2)} &= \frac{-X^2_{\rm R_C_(m-1)}}{(R_{\rm ac} + {\rm j}X_{\rm Sm}) - {\rm j}X_{\rm R_C_(m-1)}}. \qquad (19)
\end{aligned}$$

$$\begin{aligned}
&(-X_{\rm R_C_1} + X_{\rm N_C_1})X_{\rm R_C_2}\cdot(-X_{\rm R_C_2})\cdots X_{\rm R_C_i}\cdot(-X_{\rm R_C_i})\cdots X_{\rm R_C_(m-1)}\cdot(-X_{\rm R_C_(m-1)})\\
&\quad + X_{\rm N_C_1}\cdot(-X_{\rm N_C_1})(-X_{\rm R_C_2} + X_{\rm N_C_2})\cdots X_{\rm R_C_i}\cdot(-X_{\rm R_C_i})\cdots X_{\rm R_C_(m-1)}\cdot(-X_{\rm R_C_(m-1)})\\
&\quad + \cdots + X_{\rm N_C_1}\cdot(-X_{\rm N_C_1})\cdots(-X_{\rm R_C_i} + X_{\rm N_C_i})\cdots X_{\rm R_C_(m-1)}\cdot(-X_{\rm R_C_(m-1)})\\
&\quad + \cdots + X_{\rm N_C_1}\cdot(-X_{\rm N_C_1})\cdots X_{\rm N_C_i}\cdot(-X_{\rm N_C_i})\cdots(-X_{\rm R_C_(m-2)} + X_{\rm N_C_(m-2)})X_{\rm R_C_(m-1)}\cdot(-X_{\rm R_C_(m-1)})\\
&\quad + X_{\rm N_C_1}(-X_{\rm N_C_1})X_{\rm N_C_2}(-X_{\rm N_C_2})\cdots X_{\rm N_C_i}(-X_{\rm N_C_i})\cdots(-X_{\rm R_C_(m-1)} + X_{\rm Sm})\\
&= \sum_{\rm i=1}^{\rm (m-2)}\left[\prod_{\rm x=1}^{\rm (i-1)}(-X^2_{\rm N_C_x})\cdot(-X_{\rm R_C_x} + X_{\rm N_C_x})\cdot\prod_{\rm x=(i+1)}^{\rm (m-1)}(-X^2_{\rm R_C_x})\right] + (-X_{\rm R_C_(m-1)} + X_{\rm Sm})\cdot\prod_{\rm i=1}^{\rm m-2}(-X^2_{\rm N_C_i}) = 0
\end{aligned}$$

(20)

Z_{inCC} is expected to be purely resistive and independent of the load, that is ZPA operation, which implies that the imaginary part of Z_{inCC}, $\mathrm{Im}(Z_{inCC})$, is always equal to zero for any loading conditions. In order to achieve $\mathrm{Im}(Z_{inCC}) = 0$, the general resonant condition is given by (20), shown at the bottom of the previous page. In this case, the general load-independent purely resistive input impedance (R_{inCC}) is expressed by

$$R_{inCC} = \mathrm{Re}(Z_{inCC}) = \frac{X^2_{R\_C\_1}X^2_{R\_C\_2}\cdots X^2_{R\_C\_i}\cdots X^2_{R\_C\_(m-2)}X^2_{R\_C\_(m-1)}}{R_{ac}X^2_{N\_C\_1}X^2_{N\_C\_1}\cdots X^2_{N\_C\_i}\cdots X^2_{N\_C\_(m-2)}} = \frac{\prod_{i=1}^{(m-1)} X^2_{R\_C\_i}}{R_{ac}\prod_{i=1}^{(m-2)} X^2_{N\_C\_i}} = \frac{1}{R_{ac}|\mathbf{G}_{CC}|^2}. \tag{21}$$

So, for the higher order resonant circuit, the load-independent CC output with the ZPA operation is achieved under the resonant conditions of (16) and (20).

D. General Load-Independent CV Output Mode With Load-Independent ZPA

Similarly, when the sums of the two reactances of all L-section matching networks in Fig. 5(b) are defined as

$$\begin{aligned} X_{S1} + X_{P1V1} &= X_{P1V2} + X_{S2V1} = X_{S2V2} + X_{P2V1} = \cdots \\ &= X_{SiV2} + X_{PiV1} = X_{PiV2} + X_{S(i+1)V2} = \cdots \\ &= X_{S(m-1)V2} + X_{P(m-1)V1} = X_{P(m-1)V2} + X_{Sm} \\ &= 0 \end{aligned} \tag{22}$$

and the voltage transfer ratio $\mathbf{G}_{CV}$ can be expressed as

$$\begin{aligned} \mathbf{G}_{CV} &= \frac{\mathbf{V}_{ab\_CV}}{\mathbf{V}_{AB}} \\ &= \frac{jX_{P1V2}}{jX_{S1}}\frac{jX_{P2V2}}{jX_{S2V2}}\frac{jX_{P3V2}}{jX_{S3V2}}\cdots\frac{jX_{PiV2}}{jX_{SiV2}} \\ &\quad \cdots \frac{jX_{P(m-1)V2}}{jX_{S(m-1)V2}} \end{aligned} \tag{23}$$

$$\begin{aligned} X_{S1} &= -X_{P1V1} = X_{R\_V\_1} (\text{for reversed } L\text{-section No. } 1) \\ X_{P1V2} &= -X_{S2V1} = X_{N\_V\_1} (\text{for normal } L\text{-section No. } 1) \\ &\vdots \\ X_{SiV2} &= -X_{PiV1} = X_{R\_V\_i} (\text{for reversed } L\text{-section No. i}) \\ X_{PiV2} &= -X_{S(i+1)V1} = X_{N\_V\_i} (\text{for normal } L\text{-section No. i}) \\ &\vdots \\ X_{S(m-1)V2} &= -X_{P(m-1)V1} = X_{R\_V\_(m-1)} \\ X_{P(m-1)V2} &= -X_{Sm} = X_{R\_V\_(m-1)}. \end{aligned} \tag{24}$$

From (23), $\mathbf{G}_{CV}$ is independent of the load. It means that the load-independent CV output is realized when the higher order resonant circuit is fed by a CV supply and resonates at the conditions of (22).

Also, in order to simplify and express the regularity of the load-independent CV output characteristic, we define the unified nomenclature of all the variables in Fig. 5(b) as (24) according to (22). In (24), $X_{R\_V\_i}$ and $X_{N\_V\_i}$ represent the unified reactances of the i reversed and normal L-section networks of Fig. 5(b), respectively.

Then, the load-independent $\mathbf{G}_{CV}$ is simplified to

$$\mathbf{G}_{CV} = \frac{\mathbf{V}_{ab\_CV}}{\mathbf{V}_{AB}} = \frac{X_{N\_V\_1}}{X_{R\_V\_1}}\cdots\frac{X_{N\_V\_i}}{X_{R\_V\_i}}\cdots\frac{X_{N\_V\_(m-1)}}{X_{R\_V\_(m-1)}} = \frac{\prod_{i=1}^{(m-1)} X_{N\_V\_i}}{\prod_{i=1}^{(m-1)} X_{R\_V\_i}}. \tag{25}$$

Furthermore, according to (9), (10), and (24), the input impedance of Fig. 5(b), Z_{inCV}, is expressed as

$$Z_{inCV} = \mathrm{Re}(Z_{inCV}) + j\cdot\mathrm{Im}(Z_{inCV}) = R_{inCV} + j\cdot X_{inCV} = \frac{-X^2_{R\_V\_1}}{\frac{(Z_{V\_1} - jX_{N\_V\_1})\cdot jX_{N\_V\_1}}{Z_{V\_1}} - jX_{R\_V\_1}} \tag{26}$$

where

$$Z_{V\_1} = \frac{-X^2_{R\_V\_2}}{\frac{(Z_{V\_2} - jX_{N\_V\_2})\cdot jX_{N\_V\_2}}{Z_{V\_2}} - jX_{R\_V\_2}}$$

$$\vdots$$

$$Z_{V\_i} = \frac{-X^2_{R\_V\_(i+1)}}{\frac{(Z_{V\_(i+1)} - jX_{N\_V\_(i+1)})\cdot jX_{N\_V\_(i+1)}}{Z_{V\_(i+1)}} - jX_{R\_V\_(i+1)}}$$

$$\vdots$$

$$Z_{V\_(m-3)} = \frac{-X^2_{R\_V\_(m-2)}}{\frac{(Z_{V\_(m-2)} - jX_{N\_V\_(m-2)})\cdot jX_{N\_V\_(m-2)}}{Z_{V\_(m-2)}} - jX_{R\_V\_(m-2)}}$$

$$\begin{aligned} &(-X_{R\_V\_1} + X_{N\_V\_1})X_{R\_V\_2}\cdot(-X_{R\_V\_2})\cdots X_{R\_V\_i}\cdot(-X_{R\_V\_i})\cdots X_{R\_V\_(m-1)}\cdot(-X_{R\_V\_(m-1)}) \\ &\quad + X_{N\_V\_1}\cdot(-X_{N\_V\_1})(-X_{R\_V\_2} + X_{N\_V\_2})\cdots X_{R\_V\_i}\cdot(-X_{R\_V\_i})\cdots X_{R\_V\_(m-1)}\cdot(-X_{R\_V\_(m-1)}) \\ &\quad + \cdots + X_{N\_V\_1}\cdot(-X_{N\_V\_1})\cdots(-X_{R\_V\_i} + X_{N\_V\_i})\cdots X_{R\_V\_(m-1)}\cdot(-X_{R\_V\_(m-1)}) \\ &\quad + \cdots + X_{N\_V\_1}\cdot(-X_{N\_V\_1})\cdots X_{N\_V\_i}\cdot(-X_{N\_V\_i})\cdots(-X_{R\_V\_(m-2)} + X_{N\_V\_(m-2)})X_{R\_V\_(m-1)}\cdot(-X_{R\_V\_(m-1)}) \\ &= \sum_{i=1}^{(m-2)}\left[\prod_{x=1}^{(i-1)}\left(-X^2_{N\_V\_x}\right)(-X_{R\_V\_x} + X_{N\_V\_x})\prod_{x=(i+1)}^{(m-1)}\left(-X^2_{R\_V\_x}\right)\right] = 0 \end{aligned} \tag{28}$$

TABLE I
SUMMARY OF THE PROPOSED METHODOLOGY FOR AN ARBITRARY HIGHER ORDER RESONANT CIRCUIT

Features	CC output with ZPA	CV output with ZPA
An arbitrary higher-order resonant circuit	Fig. 3	
Equivalent circuits	Fig. 5(a)	Fig. 5(b)
Equivalent variable expressions	(11) and (12)	(13)
Resonant methods for achieving load-independent CC and CV outputs	(16)	(24)
General mathematical models of constant output current and voltage	(17)	(25)
Resonant methods for achieving load-independent ZPA	(16) and (20)	(24) and (28)
General mathematical models of purely resistive input impedances	(21)	(29)

$$Z_{\text{V\_(m-2)}} = \frac{-X_{\text{R\_V\_(m-1)}}^2}{\dfrac{(R_{\text{ac}} - \text{j}X_{\text{N\_V\_(m-1)}}) \cdot \text{j}X_{\text{N\_V\_(m-1)}}}{R_{\text{ac}}} - \text{j}X_{\text{R\_V\_(m-1)}}}. \tag{27}$$

Z_{inCV} is expected to be purely resistive and independent of the load, that is the ZPA operation. It means that $\text{Im}(Z_{\text{inCV}})$ is always equal to zero. The general resonant method given by (28), shown at the bottom of the previous page, is derived from $\text{Im}(Z_{\text{inCV}}) = 0$. In this case, the general load-independent purely resistive input impedance R_{inCV} is expressed as

$$\begin{aligned} R_{\text{inCV}} &= \text{Re}(Z_{\text{inCV}}) \\ &= \frac{R_{\text{ac}} X_{\text{R\_V\_1}}^2 X_{\text{R\_V\_2}}^2 \cdots X_{\text{R\_C\_i}}^2 \cdots X_{\text{R\_V\_(m-1)}}^2}{X_{\text{N\_V\_1}}^2 X_{\text{N\_V\_1}}^2 \cdots X_{\text{N\_V\_i}}^2 \cdots X_{\text{N\_V\_(m-1)}}^2} \\ &= \frac{R_{\text{ac}} \prod_{\text{i=1}}^{(\text{m}-1)} X_{\text{R\_V\_i}}^2}{\prod_{\text{i=1}}^{(\text{m}-1)} X_{\text{N\_V\_i}}^2} = \frac{R_{\text{ac}}}{|\mathbf{G}_{\text{CV}}|^2}. \end{aligned} \tag{29}$$

So, for the arbitrary higher order resonant circuit, the load-independent CV output with the ZPA operation is achieved under the resonant conditions of (24) and (28).

As aforementioned, from (17) and (25), respectively, the load-independent CC and CV outputs are achieved when the higher order resonant circuit is fed by a CV source system and resonates at the conditions of (16) and (24). Furthermore, from (21) and (29), the input impedances in CC and CV output modes are purely resistive and independent of the load. It means that for a CV-fed higher order resonant circuit, the load-independent CC and CV output modes with ZPA conditions are obtained with the proposed methodology. Table I summarizes the proposed methodology.

III. APPLICATIONS OF THE PROPOSED METHODOLOGY IN WPT SYSTEMS

As mentioned in Section II-A, all compensation topologies in IPT and CPT systems have essence of higher order resonant circuits. So, according to the proposed methodology, we can easily analyze the load-independent CC and CV output modes with ZPA operations for any compensation topologies in IPT and CPT systems. In this article, a CV-fed *LCC*-series topology, which is shown in Fig. 2(b), is applied here in detail to demonstrate the proposed methodology. In Fig. 2(b), the primary *LCC* network consists of L_{ps}, C_{pp}, and C_{ps}, and C_{ss} represents the secondary compensation capacitor.

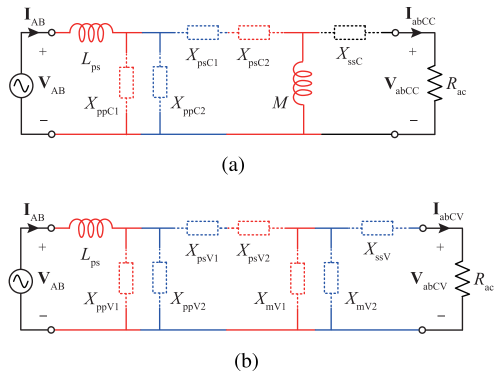

Fig. 6. Equivalent circuits of the *LCC*-series topology for achieving (a) CC output with ZPA and (b) CV output with ZPA.

A. Load-Independent CC Mode With ZPA of the LCC-Series Topology

According to the analysis in Section II-C, the *LCC*-series topology shown in Fig. 2(b) should be modeled as Fig. 6(a), which is a series-connected circuit of two-stage reversed *L*-section networks, one-stage normal *L*-section network, and the series-connected reactance X_{ssC}. The detailed equivalent expressions are derived by

$$\text{j}\omega_{\text{CC}} C_{\text{pp}} = \frac{1}{\text{j}X_{\text{ppC1}}} + \frac{1}{\text{j}X_{\text{ppC2}}} \tag{30a}$$

$$\frac{1}{\text{j}\omega_{\text{CC}} C_{\text{ps}}} + \text{j}\omega_{\text{CC}}(L_{\text{p}} - M) = \text{j}X_{\text{psC1}} + \text{j}X_{\text{psC2}} \tag{30b}$$

$$\text{j}\omega_{\text{CC}}(L_{\text{s}} - M) + \frac{1}{\text{j}\omega_{\text{CC}} C_{\text{ss}}} = \text{j}X_{\text{ssC}} \tag{30c}$$

where ω_{CC} ($\omega_{\text{CC}} = 2\pi f_{\text{CC}}$) represents the resonant frequency of Fig. 6(a).

According to (16) and (17), (31) can be derived and used as the resonant methods of Fig. 6(a) to achieve the load-independent CC output. In this case, the load-independent $\mathbf{G}_{\text{CC}}$ is given by (32)

$$\omega_{\text{CC}} L_{\text{ps}} + X_{\text{ppC1}} = X_{\text{ppC2}} + X_{\text{psC1}} = X_{\text{psC2}} + \omega_{\text{CC}} M = 0 \tag{31}$$

$$\mathbf{G}_{\text{CC}} = \frac{\mathbf{I}_{\text{abCC}}}{\mathbf{V}_{\text{AB}}} = \frac{\text{j}X_{\text{ppC2}}}{\text{j}\omega_{\text{CC}} L_{\text{ps}}} \frac{1}{\text{j}X_{\text{psC2}}}. \tag{32}$$

Furthermore, according to (20), the resonant condition for achieving ZPA condition and the corresponding purely resistive input impedance of Fig. 6(a) are expressed as

$$(X_{\mathrm{ppC1}}+X_{\mathrm{ppC2}})X_{\mathrm{psC2}}(\omega_{\mathrm{CC}}M) + X_{\mathrm{ppC2}}X_{\mathrm{psC1}}(\omega_{\mathrm{CC}}M+X_{\mathrm{ssC}})=0 \tag{33}$$

$$R_{\mathrm{inCC}} = \mathrm{Re}(Z_{\mathrm{inCC}}) = \frac{\omega_{\mathrm{CC}}^2 L_{\mathrm{ps}}^2 X_{\mathrm{psC2}}^2}{R_{\mathrm{ac}} X_{\mathrm{ppC2}}^2} = \frac{1}{R_{\mathrm{ac}}|\mathbf{G}_{\mathrm{CC}}^2|}. \tag{34}$$

B. Load-Independent CV Mode With ZPA of the LCC-Series Topology

Based on the analysis in Section II-D, the LCC-series topology should be equivalent to Fig. 6(b) to investigate its load-independent CV output mode and ZPA condition. Fig. 6(b) consists of two-stage reverse L-section networks and two-stage normal L-section networks in series. From Figs. 2(b)–6(b), the equivalent variables are expressed by the following:

$$\mathrm{j}\omega_{\mathrm{CV}}C_{\mathrm{pp}} = \frac{1}{\mathrm{j}X_{\mathrm{ppV1}}} + \frac{1}{\mathrm{j}X_{\mathrm{ppV2}}} \tag{35a}$$

$$\frac{1}{\mathrm{j}\omega_{\mathrm{CV}}C_{\mathrm{ps}}} + \mathrm{j}\omega_{\mathrm{CV}}(L_{\mathrm{p}}-M) = \mathrm{j}X_{\mathrm{psV1}} + \mathrm{j}X_{\mathrm{psV2}} \tag{35b}$$

$$\frac{1}{\mathrm{j}\omega_{\mathrm{CV}}M} = \frac{1}{\mathrm{j}X_{\mathrm{mV1}}} + \frac{1}{\mathrm{j}X_{\mathrm{mV2}}} \tag{35c}$$

$$\mathrm{j}\omega_{\mathrm{CV}}(L_{\mathrm{s}}-M) + \frac{1}{\mathrm{j}\omega_{\mathrm{CV}}C_{\mathrm{ss}}} = \mathrm{j}X_{\mathrm{ssV}} \tag{35d}$$

where ω_{CV} ($\omega_{\mathrm{CV}} = 2\pi f_{\mathrm{CV}}$) represents the resonant frequency of Fig. 6(b).

According to (24) and (25), when

$$\omega_{\mathrm{CV}}L_{\mathrm{ps}} + X_{\mathrm{ppV1}} = X_{\mathrm{ppV2}} + X_{\mathrm{psV1}} = X_{\mathrm{psV2}} + X_{\mathrm{mV1}} = X_{\mathrm{mV2}} + X_{\mathrm{ssV}} = 0 \tag{36}$$

the load-independent $\mathbf{G}_{\mathrm{CV}}$ is derived as

$$\mathbf{G}_{\mathrm{CV}} = \frac{\mathbf{V}_{\mathrm{abCV}}}{\mathbf{V}_{\mathrm{AB}}} = \frac{\mathrm{j}X_{\mathrm{ppV2}}}{\mathrm{j}\omega_{\mathrm{CV}}L_{\mathrm{ps}}}\frac{\mathrm{j}X_{\mathrm{mV2}}}{\mathrm{j}X_{\mathrm{psV2}}}. \tag{37}$$

In addition, to ensure ZPA operation in the CV mode, the following resonant condition should be satisfied according to (28):

$$(X_{\mathrm{ppV1}}+X_{\mathrm{ppV2}})X_{\mathrm{psV2}}X_{\mathrm{mV1}} + X_{\mathrm{ppV2}}X_{\mathrm{psV1}}(X_{\mathrm{mV1}}+X_{\mathrm{mV2}})=0 \tag{38}$$

and according to (29), the purely resistive input impedance R_{inCV} is expressed as

$$R_{\mathrm{inCV}} = \mathrm{Re}(Z_{\mathrm{inCV}}) = \frac{R_{\mathrm{ac}}\omega_{\mathrm{CV}}^2 L_{\mathrm{ps}}^2 X_{\mathrm{psV2}}^2}{X_{\mathrm{ppV2}}^2 X_{\mathrm{mV2}}^2} = \frac{R_{\mathrm{ac}}}{|\mathbf{G}_{\mathrm{CV}}^2|}. \tag{39}$$

IV. Evaluations

The proposed analysis methodology was verified with a 3.3-kW LCC-series-compensated IPT prototype. Fig. 7 shows the experimental setup. The air gap between the coupled coils is set at 20 cm for practical wireless EV charging applications. The input and output dc voltages are 400 and 320 V, respectively, and the output dc current is 10.3125 A, which conforms with the SAE J2954 standard [36]. Using the fundamental harmonic approximation (FHA) method, the ac transconductance gain (G_{CC}) and the ac voltage transfer ratio (G_{CV}) are then calculated and equal to 0.0318 and 0.8, respectively. The compensation components parameters and the resonant frequencies in CC and CV modes (f_{CC} and f_{CV}) are estimated through solving (30)–(33) and (35)–(38). In addition, the detailed design procedure is shown in Fig. 8. In addition, it should be pointed out that with the similar design procedure shown in Fig. 8, the system component parameters of arbitrary higher order resonant circuits including any compensation topologies in WPT systems can be designed by combining (11)–(13), (16), (17), (20), (24), (25), and (28). Then, the designed component values are shown in Table II. From Table II, the resonant frequencies in CC and CV modes are 90 and 82 kHz, respectively, which are also in compliance with SAE J2954 standard. Infineon IPW65R041CFD power MOSFETs are used to build the input single-phase full-bridge inverter. Also, Infineon IDP30E65D2 diodes are adopted at the secondary-side single-phase full-wave bridge rectifier.

Fig. 9 shows the simulation results of the LCC-series topology versus frequency. It can be seen that the transconductance

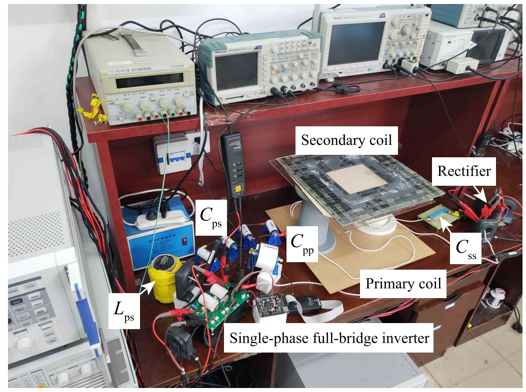

Fig. 7. Experimental setup of the IPT system.

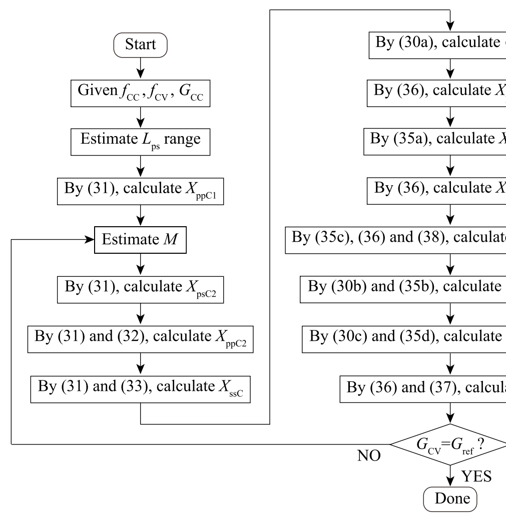

Fig. 8. Parameter design procedure of the LCC-series topology.

TABLE II
SYSTEM PARAMETERS

Parameters	Value	Parameters	Value
V_{in}	400 V	V_{o}	320 V
I_{o}	10.3125 A	L_{p}	453 μH
L_{s}	453 μH	k	0.142
L_{ps}	120.40 μH	C_{pp}	46.91 nF
C_{ps}	10.11 nF	C_{ss}	7.83 nF
f_{CC}	90 kHz	f_{CV}	82 kHz

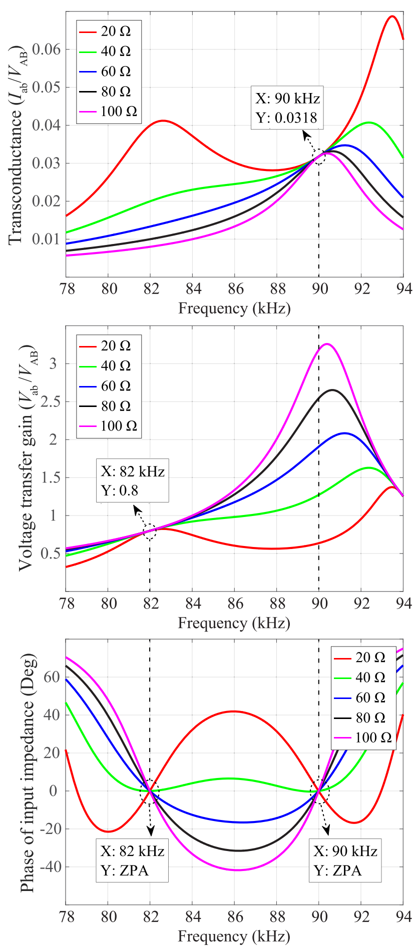

Fig. 9. Simulation results of $\mathbf{G}_{\text{CC}}$, $\mathbf{G}_{\text{CV}}$, and the phase of input impedance.

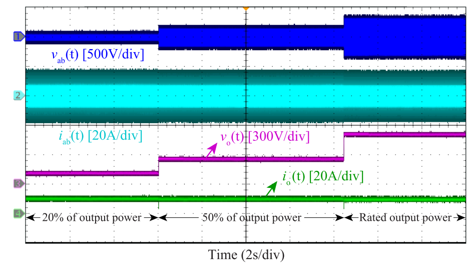

(a)

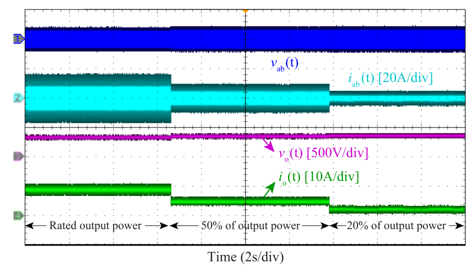

(b)

Fig. 10. Transient waveforms of $v_{\text{ab}}(t)$, $i_{\text{ab}}(t)$, $v_{\text{o}}(t)$, and $i_{\text{o}}(t)$ in (a) CC output mode and (b) CV output mode.

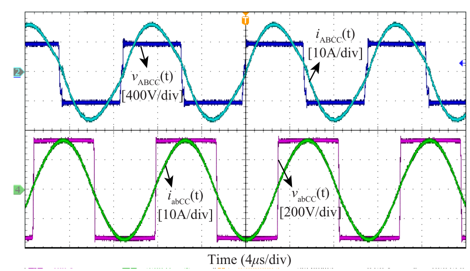

(a)

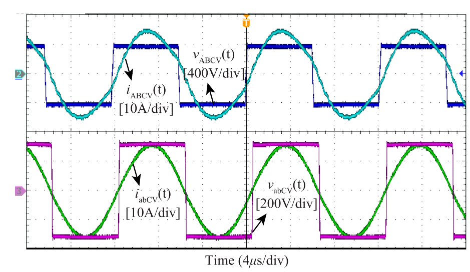

(b)

Fig. 11. Experimental waveforms of $v_{\text{AB}}(t)$, $i_{\text{AB}}(t)$, $v_{\text{ab}}(t)$, and $i_{\text{ab}}(t)$ at full-load power and in (a) CC output mode and (b) CV output mode.

is independent of the load, and the input impedance is purely resistive at any load conditions when the topology resonates at 90 kHz. The simulated transconductance is 0.0318, which is equal to the designed value. So, the load-independent CC mode with ZPA is achieved. However, the load-independent CV mode with ZPA is obtained at 82 kHz. The simulation results demonstrate the theoretical analysis in Sections III-A and III-B.

The measured transient waveforms of the output voltage $v_{\text{ab}}(t)$ and current $i_{\text{ab}}(t)$ of the compensation topology and also the rectifier output dc voltage $v_{\text{o}}(t)$ and current $i_{\text{o}}(t)$ are shown in Fig. 10(a) at 90 kHz. Fig. 10(b) shows the transient waveforms of $v_{\text{ab}}(t)$, $i_{\text{ab}}(t)$, $v_{\text{o}}(t)$, and $i_{\text{o}}(t)$ at 82 kHz. From Fig. 10(a), $i_{\text{o}}(t)$ and $i_{\text{ab}}(t)$ are always constant at the load resistance of 6.21 (20% of full-load power), 15.52, and 31.03 Ω (full-load power). It means that the load-independent current output is achieved. However, from Fig. 10(b), the CVs $v_{\text{o}}(t)$ and $v_{\text{ab}}(t)$ are achieved at any load conditions.

Fig. 11(a) and (b) shows the experimental waveforms of $v_{\text{AB}}(t)$, $i_{\text{AB}}(t)$, $v_{\text{ab}}(t)$, and $i_{\text{ab}}(t)$ at 90 (CC mode) and 82 kHz (CV mode), respectively. Fig. 12(a) and (b) shows the experimental results of $v_{\text{AB}}(t)$, $i_{\text{AB}}(t)$, $v_{\text{ab}}(t)$, and $i_{\text{ab}}(t)$ when the system operates at 50% of full-load power and CC and CV modes. From Figs. 11(a) and 12(a), $i_{\text{AB}}(t)$ is almost in phase

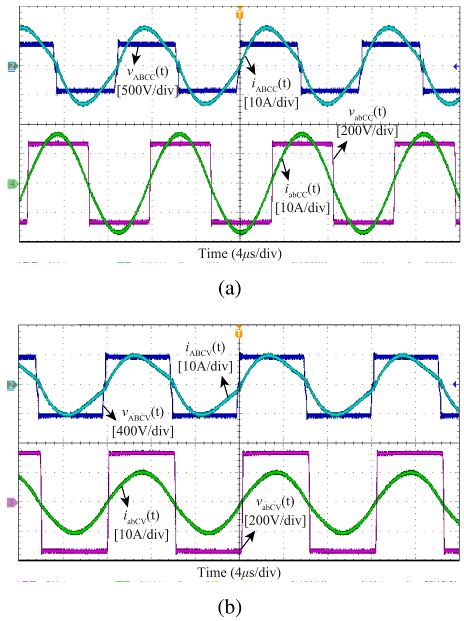

Fig. 12. Experimental waveforms of $v_{AB}(t)$, $i_{AB}(t)$, $v_{ab}(t)$, and $i_{ab}(t)$ at 50% of full-load power and in (a) CC output mode and (b) CV output mode.

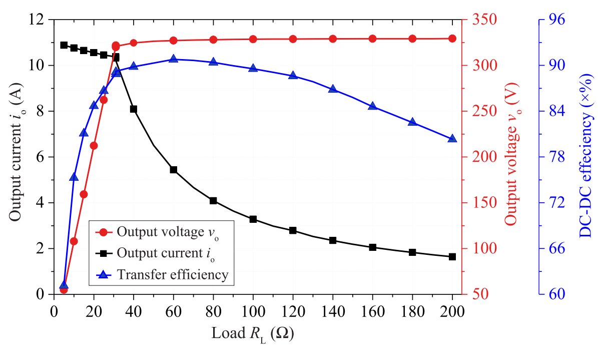

Fig. 13. Measured output dc current and voltage and the dc–dc efficiency over the full range of charging process.

with v_{AB}(t). So, according to Figs. 10(a), 11(a), and 12(a), the load-independent CC output with ZPA is achieved for the LCC-series topology. Moreover, from Figs. 11(b) and 12(b), $i_{AB}(t)$ is also almost in phase with v_{AB}(t), which match well with the analysis of (39). It means that the load-independent CV output with ZPA is obtained at 82 kHz.

Fig. 13 shows the output dc current and voltage and aslo the efficiency from the dc input of the inverter to the load over the full range of the charging process. The system operates at 90 kHz when the load resistance is continuously increased from 5 to 31.03 Ω, while the system operates at 82 kHz when the load increases from 31.03 to 200 Ω. It can be seen that the output current value is almost constant at 90 kHz and the load-independent CV output is achieved at 82 kHz. The maximum fluctuation of the output charging current in the CC mode is within 4.9%, and the maximum fluctuation of the output charging voltage is only 3.8% in the CV mode. The efficiencies in the CC and CV modes are 88.9% and 89.2% at the rated load condition. Furthermore, a peak system efficiency of 90.8% is obtained at 60 Ω and 90 kHz. Fig. 14 shows the

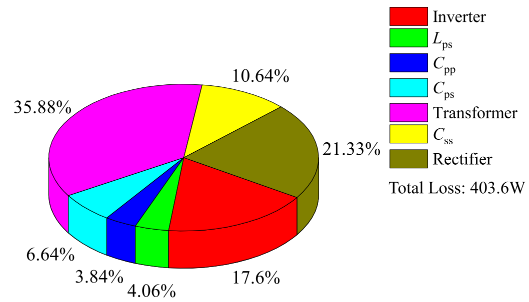

Fig. 14. Loss breakdown at full-load power at 82 kHz.

power loss breakdown based on the experimental results. The transformer loss is up to about 144.8 W, accounting for 35.88% of total losses. The large transformer loss is caused by the small coupling coefficient and the large parasitic resistances of the coupled coils.

V. Conclusion

This article proposed a general unified methodology for arbitrary higher order resonant circuits to analyze the both the load-independent CC and CV outputs with load-independent ZPA operations. The regularized mathematical models of the constant output current and voltage and the purely resistive input impedances are derived to simplify the design and optimization of the system parameters. The proposed method without adding any control algorithm and any auxiliary circuit can be generalized to investigate the load-independent output and input characteristics of some widely used resonant compensation topologies in WPT systems, including, but not limited to, LCC-series, S-SP, and double-sided LCC-compensated IPT systems, and double-sided LC, double-sided $LCLC$, and double-sided $CLLC$-compensated CPT systems. A design guideline for the practical wireless EV charging application of the LCC-series-compensated IPT system is experimentally verified by a 3.3-kW prototype.

References

[1] C. T. Rim and C. C. Mi, *Wireless Power Transfer for Electric Vehicles and Mobile Devices*. Hoboken, NJ, USA: Wiley, 2017.
[2] J. Dai and D. C. Ludois, "A survey of wireless power transfer and a critical comparison of inductive and capacitive coupling for small gap applications," *IEEE Trans. Power Electron.*, vol. 30, no. 11, pp. 6017–6029, Nov. 2015.
[3] S. Li and C. C. Mi, "Wireless power transfer for electric vehicle applications," *IEEE J. Emerg. Sel. Topics Power Electron.*, vol. 3, no. 1, pp. 4–17, Mar. 2015.
[4] D. Patil, M. K. McDonough, J. M. Miller, B. Fahimi, and P. T. Balsara, "Wireless power transfer for vehicular applications: Overview and challenges," *IEEE Trans. Transport. Electrific.*, vol. 4, no. 1, pp. 3–37, Mar. 2018.
[5] A. Ahmad, M. S. Alam, and R. Chabaan, "A comprehensive review of wireless charging technologies for electric vehicles," *IEEE Trans. Transport. Electrific.*, vol. 4, no. 1, pp. 38–63, Mar. 2018.
[6] G. Buja, M. Bertoluzzo, and K. N. Mude, "Design and experimentation of WPT charger for electric city car," *IEEE Trans. Ind. Electron.*, vol. 62, no. 12, pp. 7436–7447, Dec. 2015.
[7] R. Mai, Y. Chen, Y. Li, Y. Zhang, G. Cao, and Z. He, "Inductive power transfer for massive electric bicycles charging based on hybrid topology switching with a single inverter," *IEEE Trans. Power Electron.*, vol. 32, no. 8, pp. 5897–5906, Aug. 2017.

[8] D. H. Tran, V. B. Vu, and W. Choi, "Design of a high-efficiency wireless power transfer system with intermediate coils for the on-board chargers of electric vehicles," *IEEE Trans. Power Electron.*, vol. 33, no. 1, pp. 175–187, Jan. 2018.

[9] S. Samanta and A. K. Rathore, "Analysis and design of load-independent ZPA operation for P/S, PS/S, P/SP, and PS/SP tank networks in IPT applications," *IEEE Trans. Power Electron.*, vol. 33, no. 8, pp. 6476–6482, Aug. 2018.

[10] M. Kim, D.-M. Joo, and B. K. Lee, "Design and control of inductive power transfer system for electric vehicles considering wide variation of output voltage and coupling coefficient," *IEEE Trans. Power Electron.*, vol. 34, no. 2, pp. 1197–1208, Feb. 2019.

[11] C. Zheng *et al.*, "High-efficiency contactless power transfer system for electric vehicle battery charging application," *IEEE J. Emerg. Sel. Topics Power Electron.*, vol. 3, no. 1, pp. 65–74, Mar. 2015.

[12] C.-S. Wang, G. A. Covic, and O. H. Stielau, "Power transfer capability and bifurcation phenomena of loosely coupled inductive power transfer systems," *IEEE Trans. Ind. Electron.*, vol. 51, no. 1, pp. 148–157, Feb. 2004.

[13] Z. Huang, S. C. Wong, and C. K. Tse, "Design of a single-stage inductive-power-transfer converter for efficient EV battery charging," *IEEE Trans. Veh. Technol.*, vol. 66, no. 7, pp. 5808–5821, Jul. 2017.

[14] X. Qu, H. Han, S.-C. Wong, C. K. Tse, and W. Chen, "Hybrid IPT topologies with constant current or constant voltage output for battery charging applications," *IEEE Trans. Power Electron.*, vol. 30, no. 11, pp. 6329–6337, Nov. 2015.

[15] J. Lu, G.-R. Zhu, J. Jiang, W.-J. Li, and B. Li, "Load-independent transconductance and ZPA input for symmetrical resonant converter in IPT system," in *Proc. IEEE Energy Convers. Congr. Expo. (ECCE)*, Oct. 2017, pp. 4393–4397.

[16] X. Qu, Y. Jing, H. Han, S.-C. Wong, and C. K. Tse, "Higher order compensation for inductive-power-transfer converters with constant-voltage or constant-current output combating transformer parameter constraints," *IEEE Trans. Power Electron.*, vol. 32, no. 1, pp. 394–405, Jan. 2017.

[17] J. Hou, Q. Chen, Z. Zhang, S.-C. Wong, and K. T. Chi, "Analysis of output current characteristics for higher order primary compensation in inductive power transfer systems," *IEEE Trans. Power Electron.*, vol. 33, no. 8, pp. 6807–6821, Aug. 2018.

[18] X. Qu *et al.*, "Wide design range of constant output current using double-sided LC compensation circuits for inductive-power-transfer applications," *IEEE Trans. Power Electron.*, vol. 34, no. 3, pp. 2364–2374, Mar. 2019.

[19] S. Li, W. Li, J. Deng, T. D. Nguyen, and C. C. Mi, "A double-sided LCC compensation network and its tuning method for wireless power transfer," *IEEE Trans. Veh. Technol.*, vol. 64, no. 6, pp. 2261–2273, Jun. 2015.

[20] V.-B. Vu, D.-H. Tran, and W. Choi, "Implementation of the constant current and constant voltage charge of inductive power transfer systems with the double-sided LCC compensation topology for electric vehicle battery charge applications," *IEEE Trans. Power Electron.*, vol. 33, no. 9, pp. 7398–7410, Sep. 2018.

[21] X. Qu, H. Chu, S.-C. Wong, and C. K. Tse, "An IPT battery charger with near unity power factor and load-independent constant output combating design constraints of input voltage and transformer parameters," *IEEE Trans. Power Electron.*, vol. 34, no. 8, pp. 7719–7727, Aug. 2019. doi: 10.1109/TPEL.2018.2881207.

[22] J. Hou, Q. Chen, S.-C. Wong, C. K. Tse, and X. Ruan, "Analysis and control of series/series-parallel compensated resonant converter for contactless power transfer," *IEEE J. Emerg. Sel. Topics Power Electron.*, vol. 3, no. 1, pp. 124–136, Mar. 2015.

[23] Y. Yao, Y. Wang, X. Liu, K. Lu, and D. Xu, "Analysis and design of an S/SP compensated IPT system to minimize output voltage fluctuation versus coupling coefficient and load variation," *IEEE Trans. Veh. Technol.*, vol. 67, no. 10, pp. 9262–9272, Oct. 2018.

[24] W. Zhang and C. C. Mi, "Compensation topologies of high-power wireless power transfer systems," *IEEE Trans. Veh. Technol.*, vol. 65, no. 6, pp. 4768–4778, Jun. 2016.

[25] J. Lu, G. Zhu, D. Lin, S.-C. Wong, and J. Jiang, "Load-independent voltage and current transfer characteristics of high-order resonant network in IPT system," *IEEE J. Emerg. Sel. Topics Power Electron.*, vol. 7, no. 1, pp. 422–436, Mar. 2019.

[26] Y. H. Sohn, B. H. Choi, G.-H. Cho, and C. T. Rim, "Gyrator-based analysis of resonant circuits in inductive power transfer systems," *IEEE Trans. Power Electron.*, vol. 31, no. 10, pp. 6824–6843, Oct. 2016.

[27] F. Lu, H. Zhang, H. Hofmann, and C. C. Mi, "A double-sided LC-compensation circuit for loosely coupled capacitive power transfer," *IEEE Trans. Power Electron.*, vol. 33, no. 2, pp. 1633–1643, Feb. 2018.

[28] Y. Su, S. Xie, A. P. Hu, C. S. Tang, W. Zhou, and L. Huang, "Capacitive power transfer system with a mixed-resonant topology for constant-current multiple-pickup applications," *IEEE Trans. Power Electron.*, vol. 32, no. 11, pp. 8778–8786, Nov. 2017.

[29] Y. H. Sohn, B. H. Choi, E. S. Lee, G. C. Lim, G. H. Cho, and C. T. Rim, "General unified analyses of two-capacitor inductive power transfer systems: Equivalence of current-source SS and SP compensations," *IEEE Trans. Power Electron.*, vol. 30, no. 11, pp. 6030–6045, Nov. 2015.

[30] H. Zhang, F. Lu, H. Hofmann, W. Liu, and C. C. Mi, "A four-plate compact capacitive coupler design and LCL-compensated topology for capacitive power transfer in electric vehicle charging application," *IEEE Trans. Power Electron.*, vol. 31, no. 12, pp. 8541–8551, Dec. 2016.

[31] H. Feng, T. Cai, S. Duan, J. Zhao, X. Zhang, and C. Chen, "An LCC-compensated resonant converter optimized for robust reaction to large coupling variation in dynamic wireless power transfer," *IEEE Trans. Ind. Electron.*, vol. 63, no. 10, pp. 6591–6601, Oct. 2016.

[32] C. Xiao, D. Cheng, and K. Wei, "An LCC-C compensated wireless charging system for implantable cardiac pacemakers: Theory, experiment, and safety evaluation," *IEEE Trans. Power Electron.*, vol. 33, no. 6, pp. 4894–4905, Jun. 2018.

[33] F. Lu, H. Zhang, H. Hofmann, and C. Mi, "A double-sided LCLC-compensated capacitive power transfer system for electric vehicle charging," *IEEE Trans. Power Electron.*, vol. 30, no. 11, pp. 6011–6014, Nov. 2015.

[34] C. C. Mi, "High power capacitive power transfer for electric vehicle charging applications," in *Proc. 6th Int. Conf. Power Electron. Syst. Appl. (PESA)*, Dec. 2015, pp. 1–4.

[35] Y. Han and D. J. Perreault, "Analysis and design of high efficiency matching networks," *IEEE Trans. Power Electron.*, vol. 21, no. 5, pp. 1484–1491, Sep. 2006.

[36] "Wireless power transfer for light-duty plug-in/electric vehicles and alignment methodology," SAE Tech. Paper J2954, Nov. 2017.

Jianghua Lu (S'16) was born in Hubei, China, in 1989. He received the M.Sc. degree from the Wuhan University of Technology, Wuhan, China, in 2016, where he is currently pursuing the Ph.D. degree in electrical engineering. He is also pursuing the joint Ph.D. degree (received funding from the China Scholarship Council in 2018) with the Department of Electrical and Computer Engineering, San Diego State University, San Diego, CA, USA.

His current research interests include inductive power transfer and resonant converters.

Guorong Zhu (M'11–SM'15) received the Ph.D. degree in electrical engineering from the Huazhong University of Science and Technology, Wuhan, China, in 2009.

From 2002 to 2005, she was a Lecturer with the School of Electrical Engineering, Wuhan University of Science and Technology, Wuhan. From 2009 to 2011, she was a Research Assistant/Research Associate with the Department of Electronic and Information Engineering, Hong Kong Polytechnic University, Hong Kong. She is currently an Associate Professor with the School of Automation, Wuhan University of Technology, Wuhan. Her current research interests include wireless power transfer and the reliability of power electronics systems.

Deyan Lin (M'09) received the B.Sc. and M.A.Sc. degrees in electrical engineering from the Huazhong University of Science and Technology, Wuhan, China, in 1995 and 2004, respectively, and the Ph.D. degree from the City University of Hong Kong, Hong Kong, in 2012.

From 1995 to 1999, he was a Teaching Assistant with the Electrical Engineering Department, Jianghan University, Wuhan, where he became a Lecturer in 1999. From 2008 to 2009, he was a Senior Research Assistant with the City University of Hong Kong. He is currently a Professor with the School of Automation, Wuhan University of Technology, Wuhan, and a Post-Doctoral Fellow with the Department of Electrical and Electronic Engineering, The University of Hong Kong, Hong Kong. His current research interests include wireless power transfer, memristors, modeling, and control of gas-discharge lamps and light-emitting diode technology.

Yiming Zhang (S'13–M'16) received the B.S. and Ph.D. degrees in electrical engineering from Tsinghua University, Beijing, China, in 2011 and 2016, respectively.

He is currently a Post-Doctoral Researcher with San Diego State University, San Diego, CA, USA. His current research interests include wireless power transfer for electric vehicles and mobile phones, and resonant converters.

Jin Jiang (S'85–M'87–SM'94–F'17) received the Ph.D. degree in electrical engineering from the University of New Brunswick, Fredericton, NB, Canada, in 1989.

Since 1991, he has been with the Department of Electrical and Computer Engineering, The University of Western Ontario, London, ON, Canada, where he is currently a Senior Industrial Research Chair Professor. His current research interests include fault-tolerant control of safety-critical systems, advanced control of electrical power plants, and power systems involving renewable energy resources.

Dr. Jiang is a fellow of the Canadian Academy of Engineering. He is also a member of the International Electrotechnical Commission 45A Subcommittee to develop industrial standards on instrumentation and control for nuclear facilities. He also works closely with the International Atomic Energy Agency on modern control and instrumentation for nuclear power plants.

Chunting Chris Mi (S'00–A'01–M'01–SM'03–F'12) received the B.S.E.E. and M.S.E.E. degrees in electrical engineering from Northwestern Polytechnical University, Xi'an, China, in 1985 and 1988, respectively, and the Ph.D. degree in electrical engineering from the University of Toronto, Toronto, ON, Canada, in 2001.

He was with the University of Michigan, Dearborn, MI, USA, from 2001 to 2015. He is currently a Professor and the Chair of Electrical and Computer Engineering and also the Director of the Department of Energy (DOE)-funded Graduate Automotive Technology Education (GATE) Center for Electric Drive Transportation, San Diego State University, San Diego, CA, USA.